Fractional Quantum Anomalous Hall Effect in Multilayer Graphene

Zhengguang Lu[1]†, Tonghang Han[1]†, Yuxuan Yao[1]†, Aidan P. Reddy[1], Jixiang Yang[1], Junseok Seo[1], Kenji Watanabe[2], Takashi Taniguchi[3], Liang Fu[1], Long Ju[1]*

[1]Department of Physics, Massachusetts Institute of Technology, Cambridge, MA, USA.

[2]Research Center for Electronic and Optical Materials, National Institute for Materials Science, 1-1 Namiki, Tsukuba 305-0044, Japan

[3]Research Center for Materials Nanoarchitectonics, National Institute for Materials Science, 1-1 Namiki, Tsukuba 305-0044, Japan

*Corresponding author. Email: longju@mit.edu †These authors contributed equally to this work.

The fractional quantum anomalous Hall effect (FQAHE), the analog of the fractional quantum Hall effect[1] at zero magnetic field, is predicted to exist in topological flat bands under spontaneous time-reversal-symmetry breaking[2–6]. The demonstration of FQAHE could lead to non-Abelian anyons which form the basis of topological quantum computation[7–9]. So far, FQAHE has been observed only in twisted $MoTe_2$ at moiré filling factor $\nu > 1/2$[10–13]. Graphene-based moiré superlattices are believed to host FQAHE with the potential advantage of superior material quality and higher electron mobility. Here we report the observation of integer and fractional QAH effects in a rhombohedral pentalayer graphene/hBN moiré superlattice. At zero magnetic field, we observed plateaus of quantized Hall resistance $R_{xy} = \frac{h}{\nu e^2}$ at ν = 1, 2/3, 3/5, 4/7, 4/9, 3/7 and 2/5 of the moiré superlattice respectively, accompanied by clear dips in the longitudinal resistance R_{xx}. R_{xy} equals $\frac{2h}{e^2}$ at $\nu = 1/2$ and varies linearly with ν — similar to the composite Fermi liquid (CFL) in the half-filled lowest Landau level at high magnetic fields[14–16]. By tuning the gate displacement field D and ν, we observed phase transitions from CFL and FQAH states to other correlated electron states. Our system provides an ideal platform for exploring charge fractionalization and (non-Abelian) anyonic braiding at zero magnetic field[7–9,17–19], especially considering a lateral junction between FQAHE and superconducting regions in the same device[20–22].

The fractional quantum Hall effect observed in conventional two-dimensional electron gas (2DEGs) at the semiconductor interface is a classic example of intertwined electron correlation and topology effects in

condensed matter physics[1]. It has been proposed that similar exotic states could exist at zero magnetic field, by engineering flat electronic bands with non-zero Chern numbers [2–6]. As a precursor of FQAHE, the integer quantum anomalous Hall effect (IQAHE) has been conceived[23] and realized in magnetic topologic insulators and the moiré superlattice made of two-dimensional materials[24–27]. Recently, FQAHE has been proposed in twisted transition metal dichalcogenides (TMD) moiré superlattices[28–32] and observed in twisted $MoTe_2$ (t-$MoTe_2$) at filling factors $\nu > 1/2$[10–13]. Graphene-based moiré superlattices have also been proposed to host FQAH states[33–38], and could potentially show a plethora of fractional states due to the fewer defects in graphene lattice than in TMD lattices. Although fractional Chern insulators have been observed in graphene-based moiré superlattices at high magnetic fields[39,40], observation of FQAHE in any graphene system has not been reported to date.

The moiré superlattice formed between rhombohedral graphene (RG) and hexagonal boron nitride (hBN) has been demonstrated to be a remarkable platform for emergent quantum phenomena. In the highly tunable electronic bands in crystalline multilayer RG, correlated insulators, superconductivity, Chern insulators, orbital magnetism and multiferroicity have been demonstrated (see Methods). When placed on hBN to form a moiré superlattice, RG exhibits Mott insulators, tunable ferromagnetism and Chern insulators, as well as superconductivity (see Methods). Based on a tight-binding calculation, the band dispersion at zero gate-displacement field D becomes flatter as the layer number increases from $N = 2$ to 5, while the valence band starts to suffer from increased trigonal warping with $N > 5$[41]. At non-zero Ds, states near the band edge acquire larger Berry curvatures[41,42] that enable the formation of topological flat band when a moiré potential from hBN is introduced[36,43]. Therefore, engineering topological flat bands in gate-tuned multilayer RG/hBN is a promising approach for realizing FQAHE. From an experimental point of view, the RG/hBN moiré superlattice features three advantages over twisted TMD moiré superlattices: 1. the higher material quality of graphene over TMD; 2. better electrical contact to graphene than to TMD; 3. the twist-angle inhomogeneity induces less variations of the moiré period in a hetero-bilayer moiré than in a homo-bilayer moiré. While the Chern insulator state has been observed in trilayer RG/hBN at integer moiré fillings (see Methods), FQAHE has not been found in this system so far.

Here we report observations of IQAHE and FQAHEs in a new graphene moiré system formed by pentalayer RG and hBN, as shown in Fig. 1a. While the general possibility of FQAHE in RG/hBN moiré superlattices has been suggested before[36], the pentalayer system we study has not received any concrete theoretical analysis or predictions. The superlattice period is ~11.5 nm and the twist angle is ~0.77°. We observed quantized Hall resistance $R_{xy} = \pm\frac{h}{e^2}$ at a moiré superlattice filling factor $\nu = 1$ and zero magnetic field. These states correspond to Chern numbers $C = \pm 1$. At fractional filling factors between 0 and 1, we

observed 6 states with fractionally quantized Hall resistances $R_{xy} = \frac{h}{\nu e^2}$ at zero magnetic field. We observed $R_{xy} = \frac{2h}{e^2}$ at $\nu = 1/2$ and a linear dependence of R_{xy} on ν. By tuning D, we observed phase transitions from composite Fermi liquid (CFL) to valley-polarized Fermi liquid and a correlated insulator. We have measured two devices with similar moiré superlattice periods and they both show IQAHE and FQAHE. The data presented in the main text is based on Device 1, while the data from Device 2 is included in Extended Data Figures 8&9.

Phase Diagram of the Moiré Superlattice

Figure 1b&c show the longitudinal resistance R_{xx} and transverse resistance R_{xy} as functions of charge density n_e (filling factor ν) and D measured at mixing chamber temperature T = 10 mK. R_{xx} and R_{xy} have been symmetrized and anti-symmetrized using data collected at $B = \pm 0.1$ T (see Methods and Extended Data Figure 4). While most regions on the maps show small R_{xx} and R_{xy}, large values of resistances emerge in a tilted stripe region. At small ν up to 1/2, large R_{xx} emerges, while R_{xy} shows large fluctuations around zero. At ν = 2/5 to 1, large R_{xy} emerges and gradually changes with ν. At ν = 1, 2/3, 3/5, and 2/5, R_{xx} shows local minimums while R_{xy} shows plateaus as a function of ν. As we show in the following sections, these states feature quantized R_{xy} as expected for IQAHE and FQAHEs. We note that the charge density corresponding to $\nu = 1$ in our system is about 5 times smaller than that in t-$MoTe_2$[10–13], due to the larger moiré superlattice period.

The insulating state with large R_{xx} we observed at $\nu \leq 1/2$ occupies a large continuous range of filling factor, which is distinct from correlated insulators at integer filling factors or generalized Wigner crystals at discrete fractional filling factors of moiré superlattices[44,45]. It is possible, for example, that electron crystallization happens within the flat moiré conduction band and leads to a Wigner crystal state at zero magnetic field[46]. At $D < 0$, we observed correlated insulating states at integer filling factors ν = 2, 3 and 4 (see Extended Data Figure 1). The existence of topological states and correlated insulating states at opposite Ds are consistent with previous experiments on RG/hBN moiré superlattices (see Methods). In this work, we focus on the regime of large positive displacement fields.

In the tilted stripe region, the large anomalous Hall signals indicates spontaneous valley polarization that breaks the time-reversal symmetry. As the D required to observe the anomalous Hall signal is quite high, at finite charge density, the re-distribution of charges is expected to partially screen the externally applied D. This picture may explain the slope of the striped region, in which a larger D is needed to maintain a narrow bandwidth as ν increases. The observation of IQAHE and FQAHEs at $\nu <= 1$ further suggests the presence of a topological flat band.

Fig 1d shows a moiré band structure calculated from a tight-binding model for pentalayer RG[43], with an added phenomenological superlattice potential to account for moiré effects from the nearly aligned hBN layer. For a top-to-bottom interlayer potential difference Δ = 75 meV, this model produces a $|C|$=1 lowest conduction moiré band that is extremely narrow (bandwidth < 5 meV) and isolated from other bands with a global band gap. In contrast, the lowest valence moiré band is significantly broader (bandwidth > 45 meV), topologically trivial (C = 0), and energetically overlapping with adjacent moiré bands.

Integer Quantum Anomalous Hall Effect

Figure 2 shows detailed characterizations of the anomalous Hall state at ν = 1. At D/ε_0 = 0.97 V/nm, both R_{xy} and R_{xx} exhibit hysteretic behaviors under scanned magnetic field, as shown in Fig. 2a&b. At T = 0.1 K, R_{xy} is quantized at $\frac{h}{e^2}$ at zero magnetic field, while R_{xx} is smaller than 5 Ω. R_{xy} remains quantized up to at least 1.6 K and R_{xx} remains small in the same temperature range. Figure 2c&d show the B-dependence of R_{xy} and R_{xx} in the vicinity of ν = 1 at D/ε_0 = 0.97 V/nm. The anomalous Hall state persists to B = 0 T and exhibits a wide plateau in both R_{xy} and R_{xx}. The dispersion of this state agrees well with a Chern number $C = \pm 1$ state (indicated by the dashed line) according to the Streda's formula. Starting from ~0.6 T, more dips in R_{xx} emerge and their slopes with B agree with C = 2 and 3 states (indicated by additional dashed lines). Figure 2e shows the n_e (ν) dependence of R_{xy} and R_{xx} and features a plateau of width $\Delta n_e \sim 3*10^{10}$ cm^{-2}. The quantized R_{xy} and small R_{xx} values of the state at ν = 1 exist in a wide range of D, as shown in Fig. 2f. At both higher and lower Ds, the device shows small R_{xx} and R_{xy}, except for a peak of R_{xx} during both transitions.

These observations indicate the IQAHE with $C = \pm 1$ at filling factor ν = 1. The features corresponding to C = 2 and 3 are due to integer quantum Hall effects that emerge at a low magnetic field, which demonstrates the high electron mobility of our device. The incremental change ΔC = 1 between these three features indicates that the isospin degeneracy is completely lifted at ν = 1, which corresponds to one electron per moiré unit cell. The width of the IQAHE plateau corresponds to a ~10 times smaller charge density than that in t-$MoTe_2$[11,13].

Fractional Quantum Anomalous Hall Effect

As shown by Fig. 1b&c, large anomalous Hall response is found in a wide range between ν = 2/5 and 1. Figure 3a&b show finer maps of R_{xx} and R_{xy} in this range, where additional vertical line features can be seen. To better visualize the states corresponding to these lines, we present in Fig. 3c line-cuts along the dashed lines in Fig. 3a&b. We can observe plateaus of R_{xy} at ν = 2/5, 3/7, 4/9, 4/7, 3/5 and 2/3 with the value of R_{xy} quantized at $\frac{h}{\nu e^2}$. At the same time, R_{xx} shows clear dips at these filling factors, similar to the

observations of fractional quantum Hall states in 2DEGs at high magnetic fields[1,14]. We note that the ν = 2/5 state is right next to the boundary of the anomalous Hall region, which shows a peak in R_{xx}. Nevertheless, the clear plateau of R_{xy} and dip in R_{xx} are observed at ν = 2/5. Figure 3d-f & h-j show the magnetic hysteresis scans at fractional filling factors corresponding to the states identified in Fig. 3c. For all these states, R_{xy} shows quantized values of $\frac{h}{\nu e^2}$ while R_{xx} is much smaller than R_{xy}. Lastly, Fig. 3g&k shows the Landau-fan diagram of R_{xx} in the range of $\nu < 1/2$ and $\nu > 1/2$, respectively. The dips at fractional filling factors evolve into tilted lines whose slopes agree well with the dashed lines, which are calculated based on the Streda's formula $\frac{\partial n_e}{\partial B} = \frac{\nu e}{h}$ for the corresponding filling factors. As a function of D, all FQAH states develops a plateau of R_{xy} at the corresponding quantized values (see Extended Data Figure 2) and dips of R_{xx}. The center of the R_{xy} plateau and the dips in R_{xx} shift to higher D as the filling factor increases, which agrees with the tilted stripe shape of the anomalous Hall region as shown in Fig. 1b&c.

The observations of quantized R_{xy} and the corresponding dips in R_{xx} at fractional filling factors, together with the hysteresis enclosing zero magnetic field indicate FQAH states in our graphene-based moiré superlattice. These states resemble the Jain sequence of fractional quantum Hall states[14–16], but at zero magnetic field. Compared with t-$MoTe_2$ where FQAHEs are only observed at $\nu > 1/2$[10–13], the fractional states we observed reside at both sides of the half-filling. This is likely due to the better electrical contact in graphene devices than that has been achieved in semiconductor devices at low charge densities. The narrowest plateau width of FQAH states we have observed is ~10^{10} cm^{-2}, which is about 10 times narrower than the 3/5 state observed in t-$MoTe_2$[11].

AHE and Phase Transitions at ν = 1/2

In addition to FQAHE states that have plateaus in R_{xy} and dips in R_{xx}, we observed a continuously changing anomalous Hall resistance in a wide range of filling factors from 4/9 to 4/7. Especially at around ν = 1/2, R_{xy} varies roughly linearly with n_e and ν while R_{xx} does not show any clear dips, as shown in Fig. 4a. At ν = 1/2, R_{xy} equals $\frac{2h}{e^2}$. Fig. 4b shows the hysteretic behaviors of R_{xy} and R_{xx} under a sweeping magnetic field. Figure 4c shows the D-dependence of R_{xy} and R_{xx} at fixed filling factor ν = 1/2. The value of R_{xy} spans in a plateau which is concurrent with small values of R_{xx}. At higher D, R_{xy} decreases monotonically while R_{xx} first increases and then decreases. At lower D, R_{xx} shoots up and R_{xy} shows large fluctuations in the range of 0.85 to 0.9 V/nm. At even lower D, R_{xy} becomes almost zero while R_{xx} remains at a few kΩ. At higher D than that of the $R_{xy} = \frac{2h}{e^2}$ plateau, R_{xy} decreases monotonically while R_{xx} first increases and then decreases. As shown in Fig. 4d, the state at D/ε_0 = 0.97 V/nm features small values of R_{xy} and R_{xx}, but a decent value of the Hall angle $\theta_H \sim 9.5°$ corresponding to $\tan\theta_H = \frac{R_{xy}}{R_{xx}} \sim 0.17$.

The absence of a dip in R_{xx} at $\nu = 1/2$ and the linear dependence of R_{xy} with ν in the neighborhood are distinct from FQAH states we described in the previous section and suggest the absence of a charge gap[11,47,48]. These latter properties are reminiscent of the CFL in the half-filled lowest Landau level of 2DEGs at high magnetic fields[14–16]. Starting from the zero-magnetic-field CFL state, our data suggests two distinct types of phase transitions driven by D. At the higher D side of the CFL state, the system is in a valley-polarized metallic state, due to the non-zero anomalous Hall resistance and small R_{xx}. The persistence of valley polarization and the peak of R_{xx} at intermediate Ds suggest that it is a continuous phase transition from CFL to Fermi liquid (FL). This new type of phase transition has been recently proposed by theory in FQAHE systems but was not observed in t-$MoTe_2$[49,50]. At the lower D side, we have a phase transition from CFL to our observed correlated insulator at $\nu \leq 1/2$. Our observations call for further experiments to explore both types of phase transition, which are beyond the scope of this work.

Conclusion and Outlook

We observed IQHAE at $\nu = 1$ and FQAHEs at both sides of half-filling of the first moiré conduction band. Beyond the specific moiré superlattice demonstrated here, our results indicate the great potential of similar RG/hBN systems with varied layer number, gate displacement field and twist angle for FQAHE studies—an opportunity that has been largely overlooked by theory and experiment so far. Given the high material quality, additional opportunities of researching novel quantum phase transitions, electron crystals at zero magnetic field, and behaviors of CFL in the moiré potential are within the reach of experiments[47,48]. The possibility of high-Chern-number flat bands in RG (see Methods) also points to possibly more exotic FQAH states with non-Abelian anyons for topological quantum computation[7–9]. Furthermore, the co-existence of FQAHE and superconductivity (see Methods) in graphene systems facilitates the realization of synthetic non-Abelian anyonic braiding by using a lateral junction within the same device[20–22].

References

1. Tsui, D. C., Stormer, H. L. & Gossard, A. C. Two-dimensional magnetotransport in the extreme quantum limit. *Phys Rev Lett* **48**, 1559–1562 (1982).
2. Neupert, T., Santos, L., Chamon, C. & Mudry, C. Fractional quantum Hall states at zero magnetic field. *Phys. Rev. Lett.* **106**, 236804 (2011).
3. Tang, E., Mei, J. W. & Wen, X. G. High-temperature fractional quantum Hall states. *Phys. Rev. Lett.* **106**, 236802 (2011).
4. N Regnault, B. B. Fractional Chern insulator. *Phys. Rev. X* **1**, 021014 (2011).

5. Sheng, D. N., Gu, Z. C., Sun, K. & Sheng, L. Fractional quantum Hall effect in the absence of Landau levels. *Nat. Commun.* **2**, (2011).

6. Sun, K., Gu, Z., Katsura, H. & Das Sarma, S. Nearly flatbands with nontrivial topology. *Phys Rev Lett* **106**, 236803 (2011).

7. Moore, G. & Read, N. Nonabelions in the fractional quantum hall effect. *Nucl Phys B* **360**, 362–396 (1991).

8. Wen, X. G. Non-Abelian statistics in the fractional quantum Hall states. *Phys Rev Lett* **66**, 802 (1991).

9. Nayak, C., Simon, S. H., Stern, A., Freedman, M. & Das Sarma, S. Non-Abelian anyons and topological quantum computation. *Rev Mod Phys* **80**, 1083–1159 (2008).

10. Cai, J. *et al.* Signatures of Fractional Quantum Anomalous Hall States in Twisted MoTe2. *Nature 2023* 1–3 (2023) doi:10.1038/s41586-023-06289-w.

11. Park, H. *et al.* Observation of Fractionally Quantized Anomalous Hall Effect. *Nature* (2023) doi:10.1038/S41586-023-06536-0.

12. Zeng, Y. *et al.* Thermodynamic evidence of fractional Chern insulator in moiré MoTe2. *Nature* (2023) doi:10.1038/S41586-023-06452-3.

13. Xu, F. *et al.* Observation of Integer and Fractional Quantum Anomalous Hall Effects in Twisted Bilayer MoTe2. *Phys Rev X* **13**, 031037 (2023).

14. Willett, R. *et al.* Observation of an even-denominator quantum number in the fractional quantum Hall effect. *Phys Rev Lett* **59**, 1776 (1987).

15. Jain, J. K. Composite-fermion approach for the fractional quantum Hall effect. *Phys Rev Lett* **63**, 199 (1989).

16. Halperin, B. I., Lee, P. A. & Read, N. Theory of the half-filled Landau level. *Phys Rev B* **47**, 7312 (1993).

17. Nakamura, J., Liang, S., Gardner, G. C. & Manfra, M. J. Direct observation of anyonic braiding statistics. *Nature Physics 2020 16:9* **16**, 931–936 (2020).

18. Bartolomei, H. *et al.* Fractional statistics in anyon collisions. *Science* **368**, 173–177 (2020).

19. Kundu, H. K., Biswas, S., Ofek, N., Umansky, V. & Heiblum, M. Anyonic interference and braiding phase in a Mach-Zehnder interferometer. *Nat Phys* **19**, 515–521 (2023).

20. Lindner, N. H., Berg, E., Refael, G. & Stern, A. Fractionalizing majorana fermions: Non-abelian statistics on the edges of abelian quantum hall states. *Phys Rev X* **2**, 041002 (2012).

21. Clarke, D. J., Alicea, J. & Shtengel, K. Exotic non-Abelian anyons from conventional fractional quantum Hall states. *Nature Communications 2013 4:1* **4**, 1–9 (2013).

22. Vaezi, A. Fractional topological superconductor with fractionalized Majorana fermions. *Phys Rev B Condens Matter Mater Phys* **87**, 035132 (2013).

23. Haldane, F. D. M. Model for a quantum Hall effect without Landau levels: condensed-matter realization of the “parity anomaly”. *Phys. Rev. Lett.* **61**, 2015–2018 (1988).

24. Chang, C. Z. *et al.* Experimental observation of the quantum anomalous Hall effect in a magnetic topological insulator. *Science* **340**, 167–170 (2013).

25. Deng, Y. *et al.* Quantum anomalous Hall effect in intrinsic magnetic topological insulator. *Science* **367**, 895–900 (2020).

26. Serlin, M. *et al.* Intrinsic quantized anomalous Hall effect in a moiré heterostructure. *Science* **367**, 900–903 (2020).

27. Li, T. *et al.* Quantum anomalous Hall effect from intertwined moiré bands. *Nature* **600**, 641–646 (2021).

28. Wu, F., Lovorn, T., Tutuc, E., Martin, I. & Macdonald, A. H. Topological Insulators in Twisted Transition Metal Dichalcogenide Homobilayers. *Phys Rev Lett* **122**, 086402 (2019).

29. Li, H., Kumar, U., Sun, K. & Lin, S. Z. Spontaneous fractional Chern insulators in transition metal dichalcogenide moiré superlattices. *Phys Rev Res* **3**, L032070 (2021).

30. Devakul, T., Crépel, V., Zhang, Y. & Fu, L. Magic in twisted transition metal dichalcogenide bilayers. *Nature Communications 2021 12:1* **12**, 1–9 (2021).

31. Yu, H., Chen, M. & Yao, W. Giant magnetic field from moiré induced Berry phase in homobilayer semiconductors. *Natl Sci Rev* **7**, 12–20 (2020).

32. Crépel, V. & Fu, L. Anomalous Hall metal and fractional Chern insulator in twisted transition metal dichalcogenides. *Phys Rev B* **107**, L201109 (2023).

33. Ledwith, P. J., Tarnopolsky, G., Khalaf, E. & Vishwanath, A. Fractional Chern insulator states in twisted bilayer graphene: An analytical approach. *Phys Rev Res* **2**, 023237 (2020).

34. Abouelkomsan, A., Liu, Z. & Bergholtz, E. J. Particle-Hole Duality, Emergent Fermi Liquids, and Fractional Chern Insulators in Moiré Flatbands. *Phys Rev Lett* **124**, 106803 (2020).

35. Devakul, T. *et al.* Magic-angle helical trilayer graphene. *Sci Adv* (2023).

36. Zhang, Y. H., Mao, D., Cao, Y., Jarillo-Herrero, P. & Senthil, T. Nearly flat Chern bands in moiré superlattices. *Phys Rev B* **99**, 075127 (2019).

37. Gao, Q., Dong, J., Ledwith, P., Parker, D. & Khalaf, E. Untwisting Moiré Physics: Almost Ideal Bands and Fractional Chern Insulators in Periodically Strained Monolayer Graphene. *Phys Rev Lett* **131**, 096401 (2023).

38. Repellin, C. & Senthil, T. Chern bands of twisted bilayer graphene: Fractional Chern insulators and spin phase transition. *Phys Rev Res* **2**, (2020).

39. Spanton, E. M. *et al.* Observation of fractional Chern insulators in a van der Waals heterostructure. *Science* **360**, 62–66 (2018).

40. Xie, Y. *et al.* Fractional Chern insulators in magic-angle twisted bilayer graphene. *Nature 2021 600:7889* **600**, 439–443 (2021).

41. Koshino, M. & McCann, E. Trigonal warping and Berry's phase Nπ in ABC-stacked multilayer graphene. *Phys. Rev. B* **80**, 165409 (2009).

42. Zhang, F., Jung, J., Fiete, G. A., Niu, Q. & MacDonald, A. H. Spontaneous quantum Hall states in chirally stacked few-layer graphene systems. *Phys. Rev. Lett.* **106**, 156801 (2011).

43. Park, Y., Kim, Y., Chittari, B. L. & Jung, J. Topological flat bands in rhombohedral tetralayer and multilayer graphene on hexagonal boron nitride moire superlattices. *arXiv: 2304.12874* (2023).

44. Regan, E. C. *et al.* Mott and generalized Wigner crystal states in WSe2/WS2 moiré superlattices. *Nature 2020 579:7799* **579**, 359–363 (2020).

45. Xu, Y. *et al.* Correlated insulating states at fractional fillings of moiré superlattices. *Nature 2020 587:7833* **587**, 214–218 (2020).

46. Smoleński, T. *et al.* Signatures of Wigner crystal of electrons in a monolayer semiconductor. *Nature 2021 595:7865* **595**, 53–57 (2021).

47. Goldman, H., Reddy, A. P., Paul, N. & Fu, L. Zero-Field Composite Fermi Liquid in Twisted Semiconductor Bilayers. *Phys Rev Lett* **131**, 136501 (2023).

48. Dong, J., Wang, J., Ledwith, P. J., Vishwanath, A. & Parker, D. E. Composite Fermi Liquid at Zero Magnetic Field in Twisted MoTe2. *Phys Rev Lett* **131**, 136502 (2023).

49. Barkeshli, M. & McGreevy, J. Continuous transitions between composite Fermi liquid and Landau Fermi liquid: A route to fractionalized Mott insulators. *Phys Rev B Condens Matter Mater Phys* **86**, 075136 (2012).

50. Song, X.-Y., Zhang, Y.-H. & Senthil, T. Phase transitions out of quantum Hall states in moir\'e TMD bilayers. *arXiv: 2308.10903* (2023).

Main Figure Legends

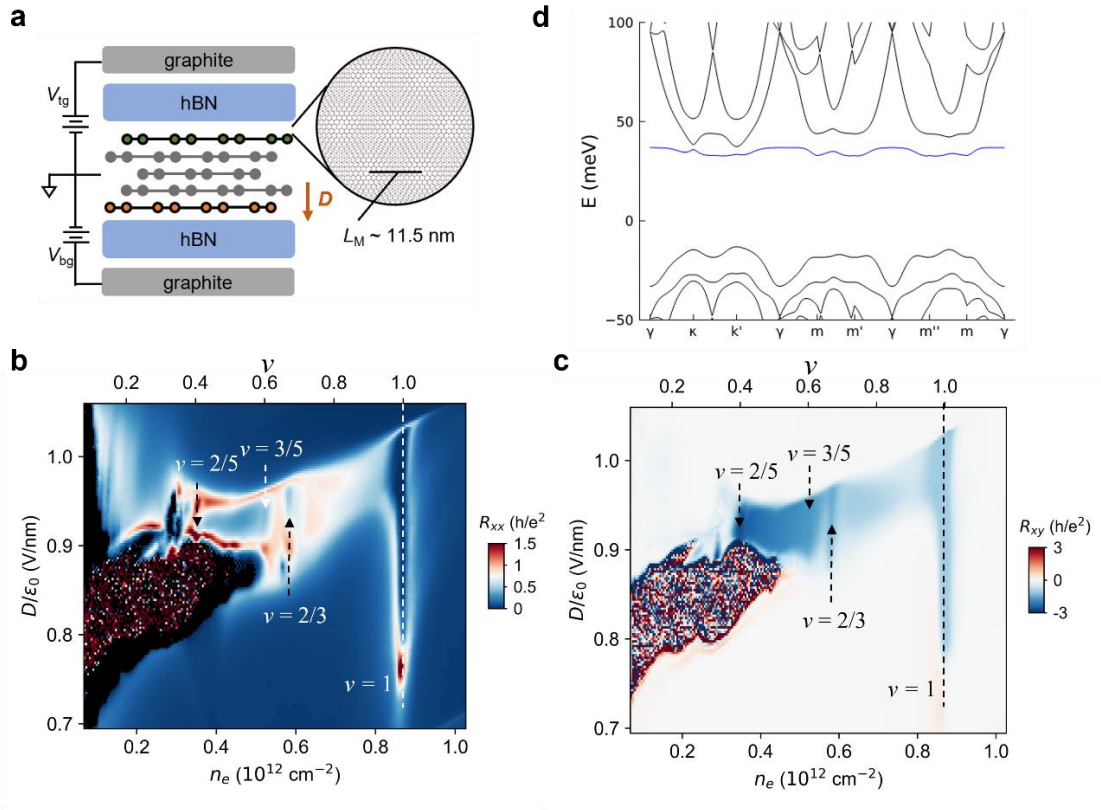

Fig. 1. Device configuration, topological flat band and phase diagram of the rhombohedral pentalayer graphene/hBN moiré superlattice. a. Schematic of the device configuration, showing a moiré superlattice between the top layer of graphene and the top hBN, with a moiré period of 11.5 nm. **b-c.** Phase diagrams of the device revealed by symmetrized R_{xx} and anti-symmetrized R_{xy} at B = ± 0.1 T as functions of n_e (ν) and D. The temperature at the mixing chamber of dilution refrigerator is 10 mK. Large anomalous Hall signals emerge in a tilted stripe region centered at D/ε_0 ~ 0.93 V/nm. Clear dips of R_{xx} can be seen at filling factors of the moiré superlattice ν = 1, 2/3, 3/5 and 2/5 (indicated by the dashed lines and arrows), where R_{xy} shows plateaus of values. **d.** Calculated band structure of our moiré superlattice with interlayer potential Δ = 75 meV, showing a flat $|C|$=1 moiré conduction band and a dispersive C=0 moiré valence band.

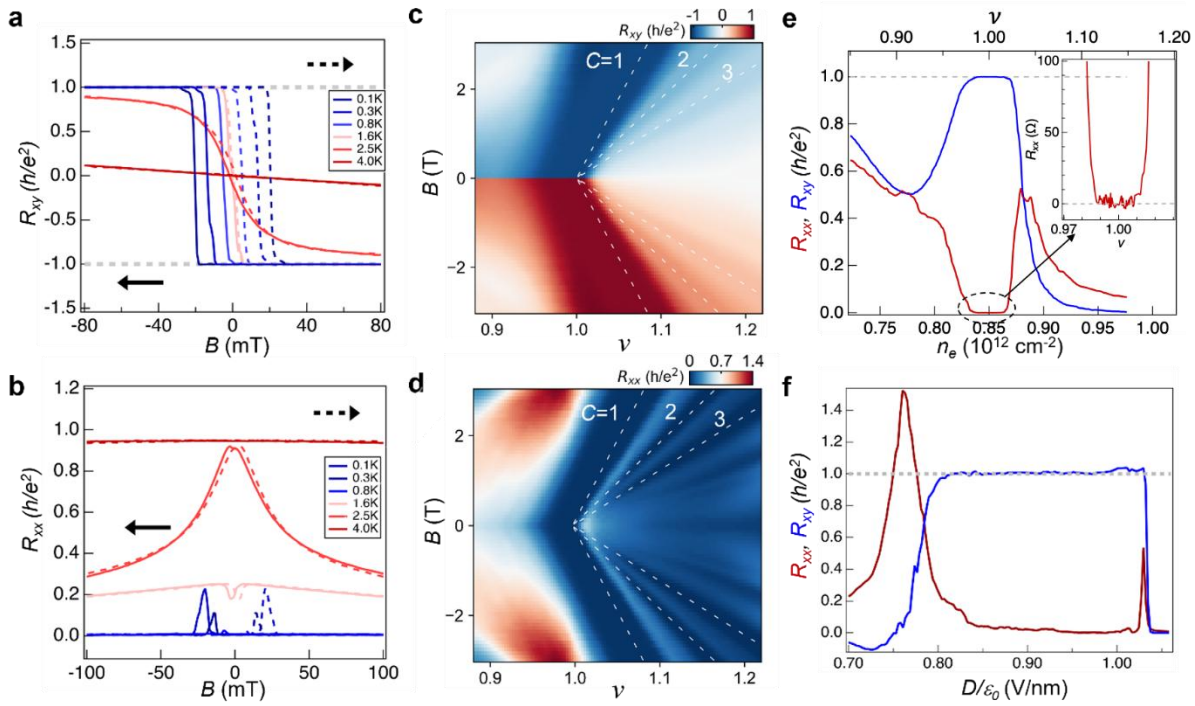

Fig. 2. Integer quantum anomalous Hall effect. a & b. Magnetic hysteresis scans of R_{xy} and R_{xx} at $\nu = 1$ and $D/\varepsilon_0 = 0.97$ V/nm and $T = 0.1$ - 4 K. Solid (dashed) lines correspond to scanning B from positive (negative) values to negative (positive) values. At 0.1 K, R_{xy} is quantized at $\pm\frac{h}{e^2}$ which corresponds to a Chern number $C = \pm 1$, while R_{xx} shows a value < 5 Ω at $B = 0$ mT. **c-d.** Landau-fan diagrams of R_{xx} and R_{xy} at $D/\varepsilon_0 = 0.97$ V/nm. The IQAH state can be seen as a wide plateau in both maps, which disperses with magnetic field with a slope that agrees well with the dashed lines (corresponding to $C = \pm 1$, as determined by the Streda's formula). At above ~0.6 T, features associated with integer quantum Hall states start to appear, corresponding to $C = \pm 2$ and 3 correspondingly as indicated by additional dashed lines. **e.** Symmetrized R_{xx} and anti-symmetrized R_{xy} (we present the positive values for convenience) as functions of ν at $T = 10$ mK and $D/\varepsilon_0 = 0.97$ V/nm, featuring quantized R_{xy} in a plateau of width ~3*10^{10} cm^{-2}. Inset: zoomed-in plot to reveal the plateau of $R_{xx} < 5$ Ω. **f.** R_{xx} and R_{xy} as a function of D at $\nu = 1$, featuring a wide plateau at ~0.8-1.03 V/nm. Moving to both higher and lower Ds, the device transitions to metallic states with small R_{xx} and R_{xy}. A peak in R_{xx} appears during both transitions.

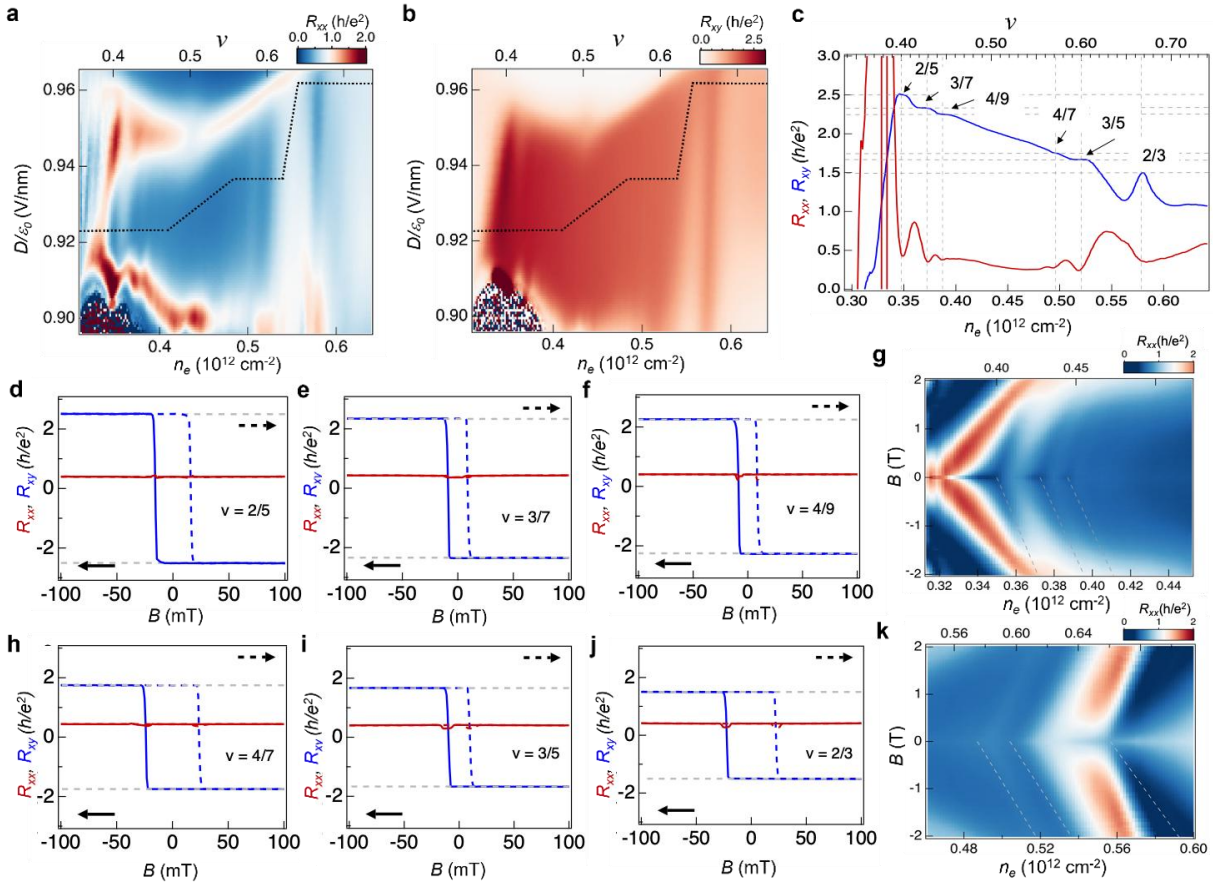

Fig. 3. Fractional quantum anomalous Hall effects. a & b. Zoomed-in diagrams of symmetrized R_{xx} and anti-symmetrized R_{xy} (we present the positive values for convenience) at $B = \pm 0.1$ T as functions of ν (n_e) and D. Fine features that could not be identified in Fig. 1d&e can be seen in the vicinity of $\nu = 1/2$, especially in the R_{xx} diagram. Data is collected using a constant voltage bias measurement. **c.** R_{xx} and R_{xy} along the dashed lines in **a** & **b,** taken with a constant current measurement. Clear plateaus of R_{xy} at $\frac{5h}{2e^2}$, $\frac{7h}{3e^2}$, $\frac{9h}{4e^2}$, $\frac{7h}{4e^2}$, $\frac{5h}{3e^2}$ and $\frac{3h}{2e^2}$ emerge at ν = 2/5, 3/7, 4/9, 4/7, 3/5 and 2/3, as indicated by the dashed lines and arrows. R_{xx} shows clear dips at the corresponding filling factors. **d-f & h-j.** Magnetic hysteresis scans of R_{xy} and R_{xx} at ν = 2/5, 3/7, 4/9, 4/7, 3/5 and 2/3, showing quantized values of $R_{xy} = \frac{h}{\nu e^2}$ and much smaller R_{xx}. **g&k.** Landau-fan diagram of R_{xx} at D/ε_0 = 0.92 V/nm. The FQAH states can be seen as tilted line features, the slopes of which agree well with the dashed lines. The slopes of dashed lines correspond to C = 2/5, 3/7 and 4/9 in **g**, and 4/7, 3/5 and 2/3 in **k** using the Streda's formula.

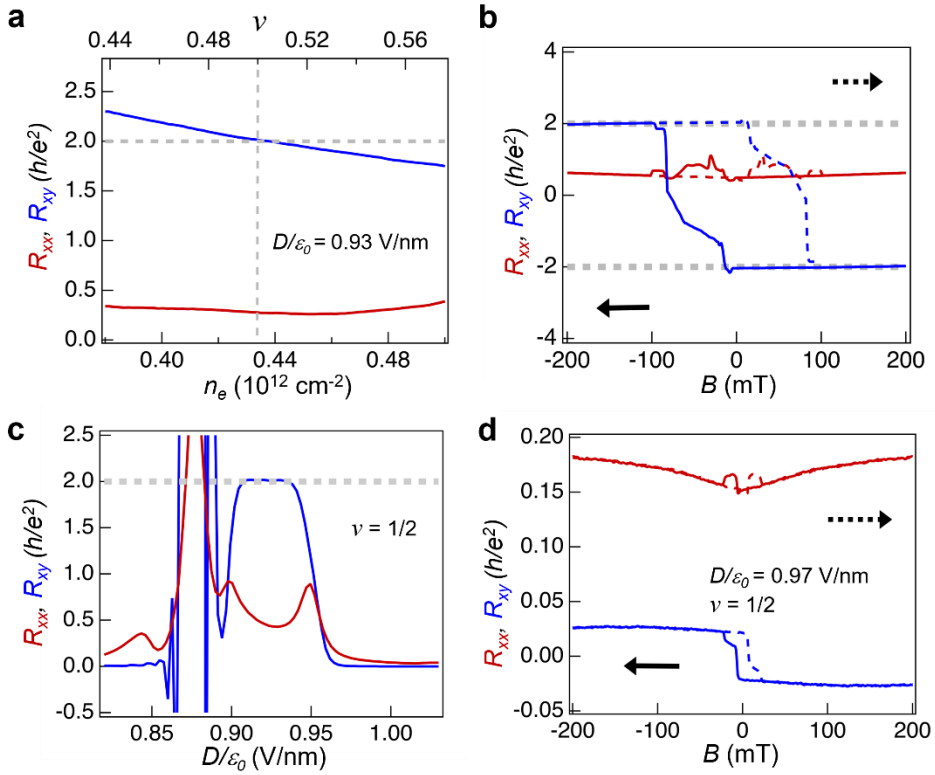

Fig. 4. Anomalous Hall effect and phase transitions at half-filling. a. Symmetrized R_{xx} and anti-symmetrized R_{xy} (we present the positive values for convenience) at B = ± 0.1 T and D/ε_0 = 0.93 V/nm in the neighborhood of half-filling. R_{xy} shows a value of $\frac{2h}{e^2}$ at ν = 1/2 and varies roughly linearly with the change of filling factor, while no dip in R_{xx} is observed. These observations resemble the signatures of composite Fermi liquid (CFL) in 2DEGs at high magnetic fields. **b.** Magnetic hysteresis scans of R_{xy} and R_{xx} at ν = 1/2, showing R_{xy} plateaus at $\pm\frac{2h}{e^2}$ and much smaller R_{xx}. **c.** R_{xy} and R_{xx} at ν = 1/2 as functions of D, showing the same R_{xy} value in a plateau spanning from 0.9 to 0.94 V/nm. At higher D, both R_{xy} and R_{xx} decrease to close to zero. At lower D, R_{xx} shoots up while R_{xy} shows large fluctuations at around zero. **d.** Magnetic hysteresis scans of R_{xy} and R_{xx} at ν = 1/2 and D/ε_0 = 0.97 V/nm, showing anomalous Hall signals and a Hall angle $\theta_H \sim 9.5°$, corresponding to $\tan\theta_H = \frac{R_{xy}}{R_{xx}} \sim 0.17$. This indicates a phase transition from CFL to valley-polarized metal at the higher D side. At the lower D side, the phase transition happens between CFL and a correlated insulating state.

Methods

Device fabrication

The pentalayer graphene and hBN flakes were prepared by mechanical exfoliation onto SiO_2/Si substrates. The rhombohedral domains of pentalayer graphene were identified using near-field infrared microscopy[51], confirmed with Raman spectroscopy and isolated by cutting with a Bruker atomic force microscope (AFM)[52]. The van der Waals heterostructure was made following a dry transfer procedure. We picked up the top hBN, graphite, middle hBN, and the pentalayer graphene using polypropylene carbonate (PPC) film and landed it on a prepared bottom stack consisting of an hBN and graphite bottom gate. The device was then etched into a Hall bar structure using standard e-beam lithography (EBL) and reactive-ion etching (RIE). We deposited Cr/Au for electrical connections to the source, drain and gate electrodes.

Previous experimental works on multilayer rhombohedral graphene

Multilayer RG with layer number > 2 has been studied heavily in experiment. In the highly tunable electronic bands in crystalline multilayer RG[53–56], correlated insulators, superconductivity, Chern insulators, orbital magnetism and multiferroicity have been demonstrated[53,56–63]. When placed on hBN to form a moiré superlattice, RG exhibits Mott insulators, tunable ferromagnetism and Chern insulators, as well as superconductivity[64–67]

Previous experiments adopted three different device configurations: 1. RG on SiO_2 substrate[53–55]; 2. Suspended RG[56,57]; 3. RG-encapsulated by hBN[58–67]. Our devices are in the third category, which balance high device quality, large parameter space enabled by high gate voltages, and multiple terminals that allow the decoupling of R_{xx} and R_{xy}. These factors all contribute to the experimental observation of FQAHE.

Transport measurement

The device was measured in a Bluefors LD250 dilution refrigerator with an electronic temperature of around 100 mK. Stanford Research Systems SR830 lock-in amplifiers were used to measure the longitudinal and Hall resistance R_{xx} and R_{xy} with an AC frequency at 17.77 Hz. For constant voltage measurement, a voltage bias of 60 uV was applied. For constant current measurement, a current bias of 2

nA was applied. Keithley 2400 source-meters were used to apply top and bottom gate voltages. Top-gate voltage V_t and bottom-gate voltage V_b are swept to adjust doping density $n_e = (C_tV_t + C_bV_b)/e$ and displacement field $D/\varepsilon_0 = (C_tV_t - C_bV_b)/2$, where C_t and C_b are top-gate and bottom-gate capacitance per area calculated from the Landau fan diagram.

Disentangling longitudinal and Hall resistance

The optical images of the two devices are shown in Extended Data Figure 1c&d. Two contacts on one side of the device did not work and were floated during the measurement. The device geometry is such that no pair of contacts allows a perfect measurement of pure R_{xy} or R_{xx}. To disentangle R_{xx} and R_{xy} in the resistance tensor, we used magnetic field symmetrization/anti-symmetrization method[26,59,68]. The longitudinal resistance and Hall resistance can be separated by using magnetic field symmetrization/anti-symmetrization method based on the fact that R_{xx} is symmetric with B, while R_{xy} is antisymmetric. Measurements performed at opposite magnetic fields (larger than the coercive field) can thus be used to extract R_{xx} and R_{xy} at $B = 0$ for the QAH states, following:

$$R_{xx}(0) = (R(B) + R(-B))/2 \qquad R_{xy}(0) = (R(B) - R(-B))/2$$

In Extended Data Figure 4. we demonstrate the field symmetrization/anti-symmetrization method step by step from the raw data to the plot we used in Fig. 1b&c as an example. For simplicity, $R_{12,34}$ corresponds to a resistance measured by applying current from contact #1 to #2 and measuring the voltage between #3 and #4. $R_{13,24}$ is measured at $B = \pm 100$mT as shown in Extended Data Figure 4a&b. The R_{xy} can be obtained by extracting the field antisymmetric part of $R_{13,24}$ or $R_{24,13}$, following:

$$R_{xy}(0) = (R_{13,24}(100\text{mT}) - R_{13,24}(-100\text{mT}))/2$$

Since the longitudinal component is symmetric respect to magnetic field, they will be cancelled by this subtraction process at the same magnitude of magnetic field but with opposite sign. Therefore, the disentangled R_{xy} could be obtained which is plotted in Extended Data Figure 4c and used in Fig. 1c. Following the same argument, resistance measurement of $R_{23,14}$ is performed at $B = \pm 100$mT as shown in Extended Data Figure 4d&e. The longitudinal resistance can be separate by following:

$$R_{xx}(0) = (R_{23,14}(100\text{mT}) + R_{23,14}(-100\text{mT}))/2$$

Since the Hall resistance is anti-symmetric respect to magnetic field, they will be perfectly removed by this summation process at opposite magnetic field. So that longitudinal resistance can be separated and plot in Extended Data Figure 4f and also shown in Fig. 1b.

In Fig. 1c and 2c we plotted (R_{xy} (0.1 T) - R_{xy} (-0.1 T))/2, while in 2e&f, 3b&c and 4a&c we plotted (R_{xy} (-0.1 T) - R_{xy} (0.1 T))/2 for the convenience of presentation.

Apart from disentangling longitudinal and Hall resistance, measurement at a magnetic field larger than the coercive field also eliminates the random fluctuations of the magnetic domains at zero magnetic field, which is typical for micro-sized devices. As shown in Extended Data Figure 6a, spikes appear randomly in all curves at B = 0 as we scan the moiré filling factor v. These fluctuations correspond to the random switching of the orbital magnetization in our micron-sized devices. At B = ± 100mT, these fluctuations are completely suppressed. We have also performed scans at even smaller magnetic fields. As shown in Extended Data Figure 6b, all the curves at B = 10mT, 50mT and 100mT overlap well. Therefore, the magnetic field of ±0.1T we used is just to avoid fluctuations, while the phenomena we observed is robust at B = 0.

Magnetic hysteresis measurements of R_{xx} and R_{xy}

The four-probe magnetic hysteresis measurements with all possible pin combinations and the results of raw data and data after processing at ν=3/5 in Extended Data Figure 5 as an example. First, we used magnetic field symmetrization/anti-symmetrization method to disentangle R_{xx} and R_{xy}. Magnetic field sweep of $R_{13,24}$ is shown as solid (dashed) line in Extended Data Figure 5a. In this case, Hall resistance can be extracted by following the field anti-symmetrization method:

$R_{xy\_solid}=(R_{13,24\_solid}(+B)-R_{13,24\_dash}(-B))/2.$ $R_{xy\_dash}=(R_{13,24\_dash}(+B)-R_{13,24\_solid}(-B))/2$

The obtained R_{xy} is plotted in Extended Data Figure 5g with anomalous Hall value equals to the quantized value at v=3/5. Based on the raw data shown in Extended Data Figure 5b, magnetic field sweep of $R_{24,13}$ can be treated in a similar way:

$R_{xy\_solid}=(R_{24,13\_solid}(+B)-R_{24,13\_dash}(-B))/2.$ $R_{xy\_dash}=(R_{24,13\_dash}(+B)-R_{24,13\_solid}(-B))/2$

The hysteresis loop after anti-symmetrization is shown in Extended Data Figure 5h.

The magnetic sweep of longitudinal resistance can be extracted based on the raw data from $R_{14,23}$ and $R_{23,14}$ measurements by following the magnetic field symmetrization method:

$R_{xx\_solid}=(R_{14,23\_solid}(+B)+R_{14,23\_dash}(-B))/2.$ $R_{xx\_dash}=(R_{14,23\_dash}(-B)+R_{14,23\_solid}(+B))/2$

$R_{xx\_solid}=(R_{23,14\_solid}(+B)+R_{23,14\_dash}(-B))/2.$ $R_{xx\_dash}=(R_{23,14\_dash}(-B)+R_{23,14\_solid}(+B))/2$

The symmetrized R_{xx} is plotted in Extended Data Figure 5i&l.

Other than relying on the symmetrization/anti-symmetrization with respect to magnetic field, we also performed symmetrization/anti-symmetrization by using Onsager reciprocal relation to better capture the

behaviors of the magnetic domain[26,59,68]. $R_{14,23}$ and its Onsager reciprocal $R_{23,14}$ are mainly contributed by R_{xx}. The symmetrization can then be performed by following:

$R_{xx\_solid}=(R_{14,23\_solid}+R_{23,14\_solid})/2.$ $R_{xx\_dash}=(R_{14,23\_dash}+R_{23,14\_dash})/2$

The hysteresis loop of the disentangled longitudinal resistance obtained by Onsager reciprocal relation is plotted in Extended Data Figure 5n. Similarly, $R_{24,13}$ and its Onsager reciprocal $R_{13,24}$ are dominated by R_{xy}. The longitudinal part can be eliminated by performing the following anti-symmetrization process:

$R_{xy\_solid}=(R_{13,24\_solid}-R_{24,13\_solid})/2.$ $R_{xy\_dash}=(R_{24,13\_dash}-R_{13,24\_dash})/2$

As we can see from Extended Data Figure 5c,f&m, no matter what symmetrization method we use, the Hall resistance value always stay quantized at $B = 0$. Since the physics we would like to address in the manuscript is not about magnetic domain, symmetrization/anti-symmetrization respect to magnetic field is used for the hysteresis loop in Fig. 2a&b, Fig. 3d-j and Fig. 4b&d.

Phenomenological model for moiré bands

We calculate the band structure shown in Fig. 1d starting from the $k \cdot p$ Hamiltonian of Ref[43] for (moiré-less) N-layer RG with N=5 and $t_0 = -2.6$ eV for nearest-neighbor intralayer hopping. Using the hBN moiré potential model of Ref[43], which only couples directly to the adjacent graphene layer, we do not obtain an isolated |C|=1 band at large displacement field. We note, however, that the nearly aligned hBN layer will induce a charge density modulation and the resulting Hartree-Fock potential will act on all layers. This motivates us to consider the following phenomenological model:

$$H = H_0(\vec{k}) + V(\vec{r})$$

where $H_0(\vec{k})$ is the moiré-less $k \cdot p$ Hamiltonian and

$$V(\vec{r}) = -2V_0 \sum_{i=1,3,5} \cos(\vec{g}_i \cdot \vec{r} + \phi)$$

is a superlattice potential that acts identically on all layers. We choose $V_0 = 10$ meV, $\phi = 0$. We note that the appearance of an isolated |C|=1 band does not rely on fine tuning of these parameters or the potential acting equally on all layers. Here the moiré reciprocal lattice vectors are $\vec{g}_1 = (\epsilon - \theta\, \hat{z}\times)(0, \frac{4\pi}{a_0\sqrt{3}})$ where $\epsilon = 0.017$ is the graphene-hBN lattice constant mismatch and we choose $\theta = 0.744\pi/180$ to achieve a moiré period $a_M = \frac{4\pi}{\sqrt{3}|\vec{g}_1|} = 11.5$ nm as determined experimentally.

Methods only references

51. Ju, L. *et al.* Topological valley transport at bilayer graphene domain walls. *Nature* **520**, 650–655 (2015).

52. Li, H. *et al.* Electrode-Free Anodic Oxidation Nanolithography of Low-Dimensional Materials. *Nano Lett* **18**, 8011–8015 (2018).

53. Bao, W. *et al.* Stacking-dependent band gap and quantum transport in trilayer graphene. *Nat. Phys.* **7**, 948–952 (2011).

54. Zhang, L., Zhang, Y., Camacho, J., Khodas, M. & Zaliznyak, I. The experimental observation of quantum Hall effect of l=3 chiral quasiparticles in trilayer graphene. *Nature Physics 2011 7:12* **7**, 953–957 (2011).

55. Zou, K., Zhang, F., Clapp, C., MacDonald, A. H. & Zhu, J. Transport studies of dual-gated ABC and ABA trilayer graphene: Band gap opening and band structure tuning in very large perpendicular electric fields. *Nano Lett* **13**, 369–373 (2013).

56. Lee, Y. *et al.* Competition between spontaneous symmetry breaking and single-particle gaps in trilayer graphene. *Nat. Commun.* **5**, (2014).

57. Myhro, K. *et al.* Large tunable intrinsic gap in rhombohedral-stacked tetralayer graphene at half filling. *2d Mater* **5**, 045013 (2018).

58. Shi, Y. *et al.* Electronic phase separation in multilayer rhombohedral graphite. *Nature 2020 584:7820* **584**, 210–214 (2020).

59. Zhou, H. *et al.* Half- and quarter-metals in rhombohedral trilayer graphene. *Nature 2021 598:7881* **598**, 429–433 (2021).

60. Zhou, H., Xie, T., Taniguchi, T., Watanabe, K. & Young, A. F. Superconductivity in rhombohedral trilayer graphene. *Nature 2021 598:7881* **598**, 434–438 (2021).

61. Han, T. *et al.* Correlated Insulator and Chern Insulators in Pentalayer Rhombohedral Stacked Graphene. *Nat. Nanotechnology* (2023).

62. Han, T. *et al.* Orbital Multiferroicity in Pentalayer Rhombohedral Graphene. *Nature* (2023).

63. Liu, K. *et al.* Interaction-driven spontaneous broken-symmetry insulator and metals in ABCA tetralayer graphene. *Nat Nanotechnol* (2023).

64. Chen, G. *et al.* Evidence of a gate-tunable Mott insulator in a trilayer graphene moiré superlattice. *Nature Physics 2019 15:3* **15**, 237–241 (2019).

65. Chen, G. *et al.* Tunable Orbital Ferromagnetism at Noninteger Filling of a Moiré Superlattice. *Nano Lett* **22**, 238–245 (2022).

66. Chen, G. *et al.* Tunable correlated Chern insulator and ferromagnetism in a moiré superlattice. *Nature* **579**, 56–61 (2020).

67. Chen, G. *et al.* Signatures of tunable superconductivity in a trilayer graphene moiré superlattice. *Nature* **572**, 215–219 (2019).

68. Sample, H. H., Bruno, W. J., Sample, S. B. & Sichel, E. K. Reverse-field reciprocity for conducting specimens in magnetic fields. *J Appl Phys* **61**, 1079–1084 (1987).

Acknowledgments

We acknowledge helpful discussions with X.G. Wen, T. Senthil, P. Lee, F. Wang and R. Ashoori. We thank D. Laroche for assistance with early investigation of a related sample. L.J. acknowledges support from a Sloan Fellowship. Work by T.H., J.Y. and J.S. was supported by NSF grant no. DMR- 2225925. The device fabrication of this work was supported by the STC Center for Integrated Quantum Materials, NSF grant no. DMR-1231319 and was carried out at the Harvard Center for Nanoscale Systems and MIT.Nano. Part of the device fabrication was supported by USD(R&E) under contract no. FA8702-15-D-0001. K.W. and T.T. acknowledge support from the JSPS KAKENHI (Grant Numbers 20H00354, 21H05233 and 23H02052) and World Premier International Research Center Initiative (WPI), MEXT, Japan. A.R. was supported by the Air Force Office of Scientific Research (AFOSR) under award FA9550-22-1-0432. L.F. was supported by the STC Center for Integrated Quantum Materials (CIQM) under NSF award no. DMR-1231319.

Author Contributions

L.J. supervised the project. Z.L. and T.H. performed the DC magneto-transport measurement. T.H. and Y.Y. fabricated the devices. J.Y., J.S., Z.L. and T.H. helped with installing and testing the dilution refrigerator. A.R. and L.F. performed the calculations. K.W. and T.T. grew hBN crystals. All authors discussed the results and wrote the paper.

Competing Interests The authors declare no competing interests.

Correspondence and requests for materials should be addressed to Long Ju.

Data availability The data shown in the main figures are available from https://doi.org/10.7910/DVN/T4QPNP. Other data that support the findings of this study are available from the corresponding authors upon reasonable request.

Extended Data Figure Legends

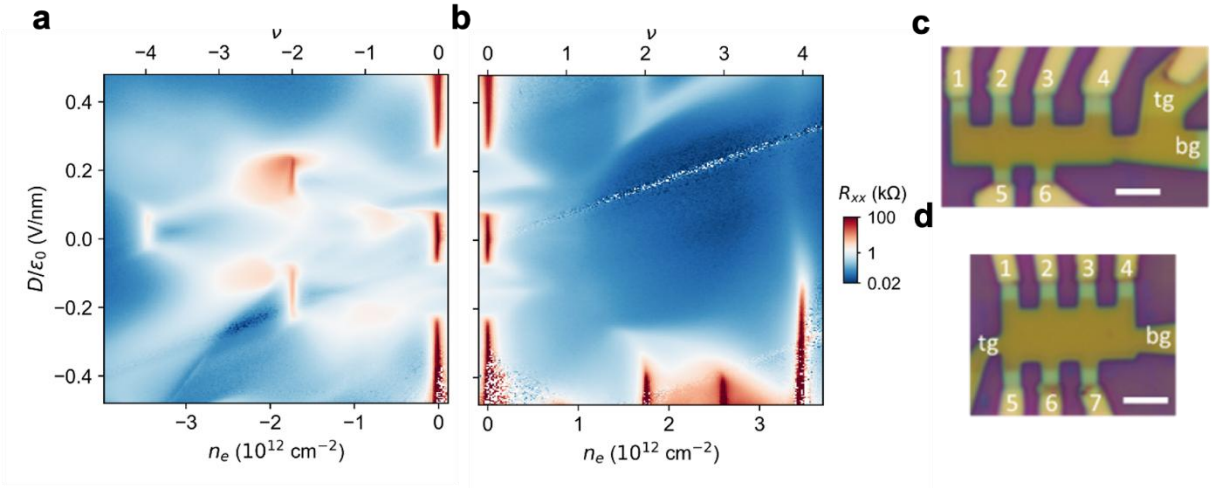

Extended Data Figure 1. Phase diagram and optical micrographs of our devices. a&b corresponds to the hole-doping and electron-doping sides, respectively. The hole side shows resistive states at filling factors ν = -2 and –4, while the electron side shows correlated insulating states at ν = 2, 3 and 4 at D < 0—opposite side of D at which we observed IQAHE and FQAHEs. **c.** Device 1 from which the data in the main text is taken. Scale bar: 3μm **d.** Device 2, the data of which is included in Extended Data Fig. 8&9. Scale bar:3μm.

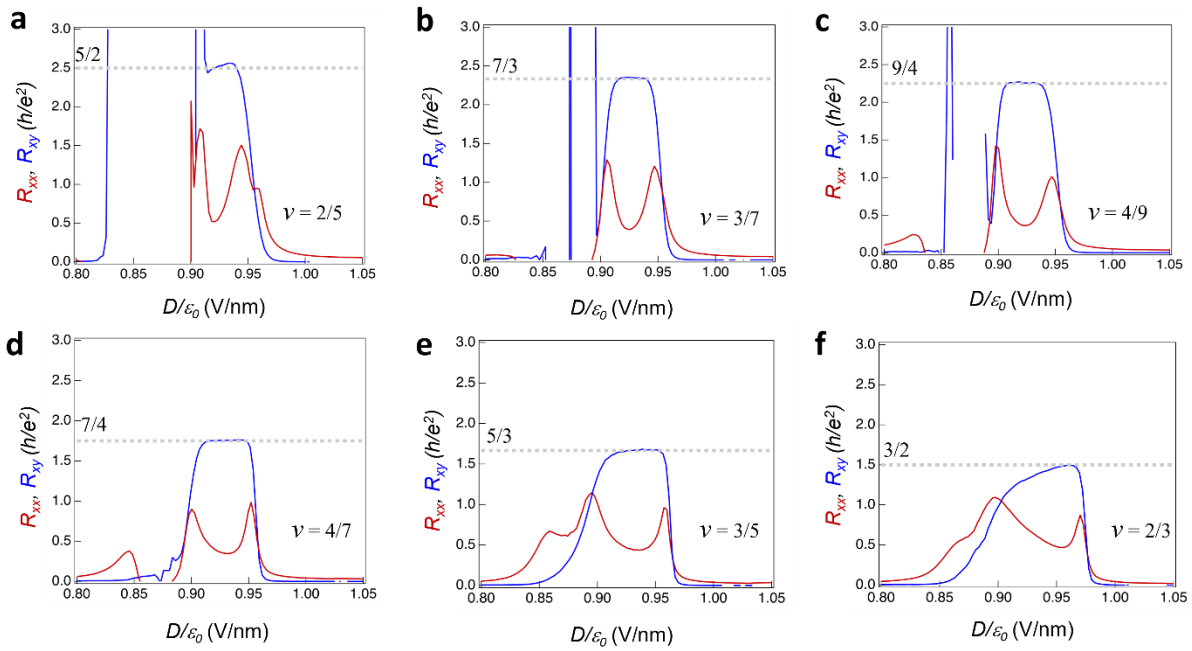

Extended Data Figure 2. Gate displacement field dependence of R_{xx} and R_{xy} at fractional filling factors for Device 1. Each FQAH state shows quantized R_{xy} in a range of D, while the center of this range for different states shifts with the filling factor. The D corresponding to the minimum of R_{xx} also shifts with the filling factor in the same direction.

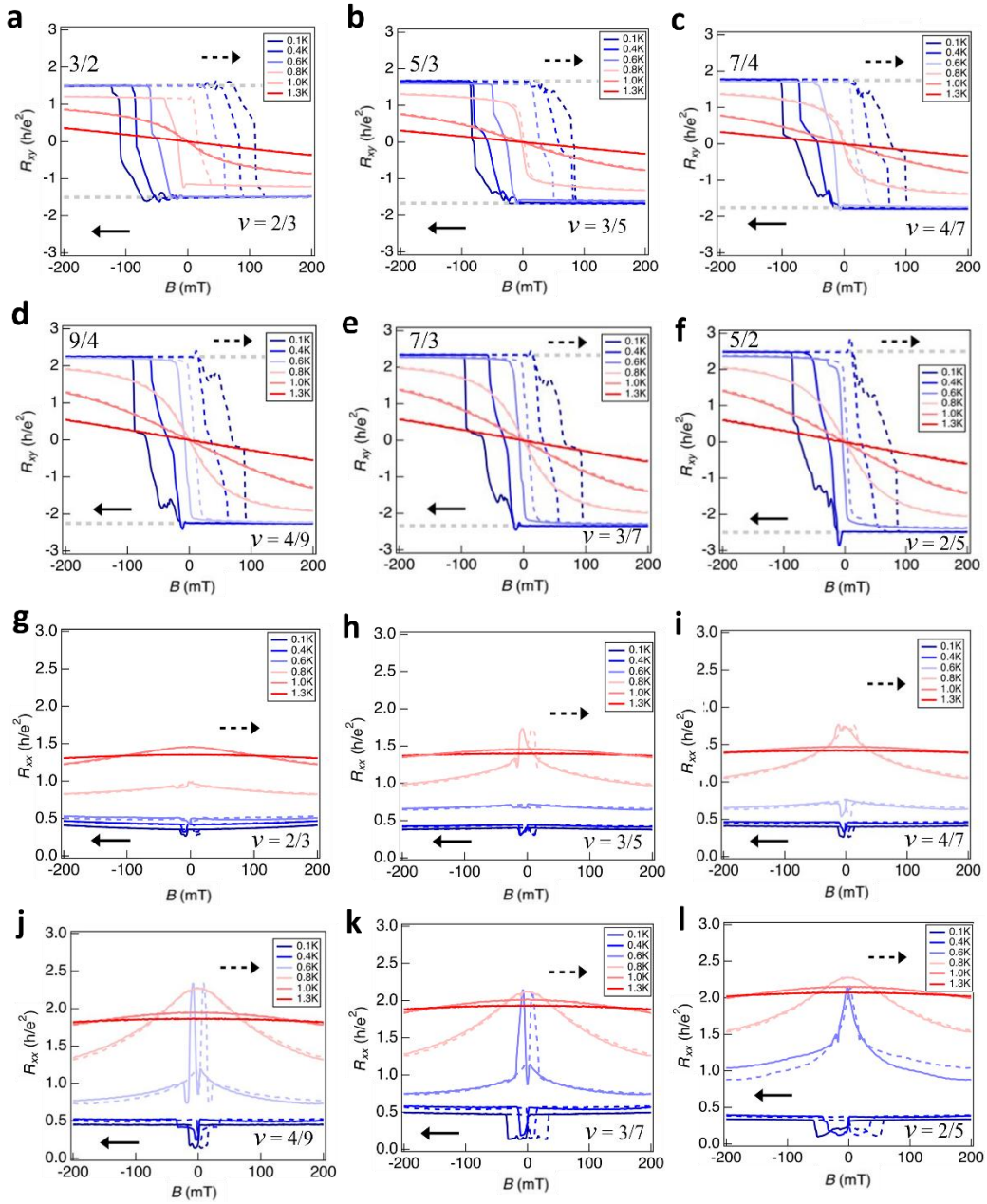

Extended Data Figure 3. Temperature dependence of FQAH states. a-f. Temperature dependence of R_{xy}. All states still remain quantized at 400 mK. **g-l.** Temperature dependence of R_{xx}.

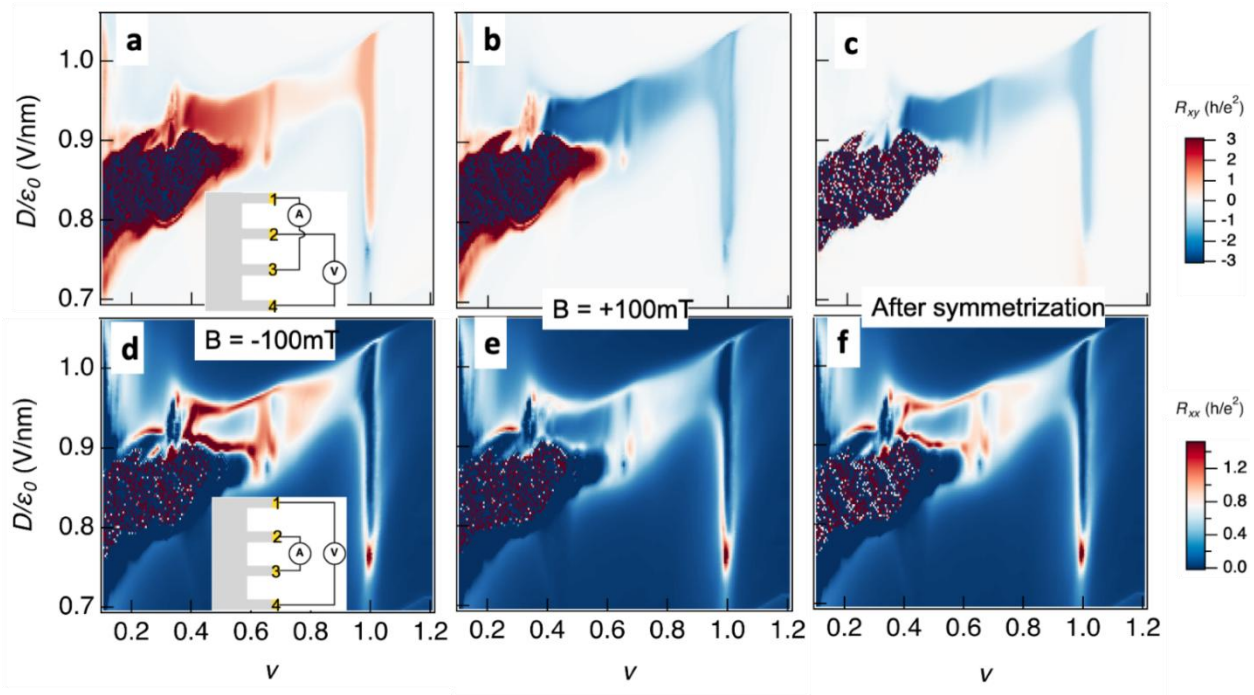

Extended Data Figure 4. Symmetrization/anti-symmetrization method to obtain Fig. 1b&c. a,b&d,e. Raw data of $R_{13,24}$ and $R_{23,14}$ measured as functions of displacement field and moiré filling factor ν at B=±100mT. The insets show the measurement pin configurations. **c&f.** R_{xy} and R_{xx} obtained after the symmetrization/anti-symmetrization process.

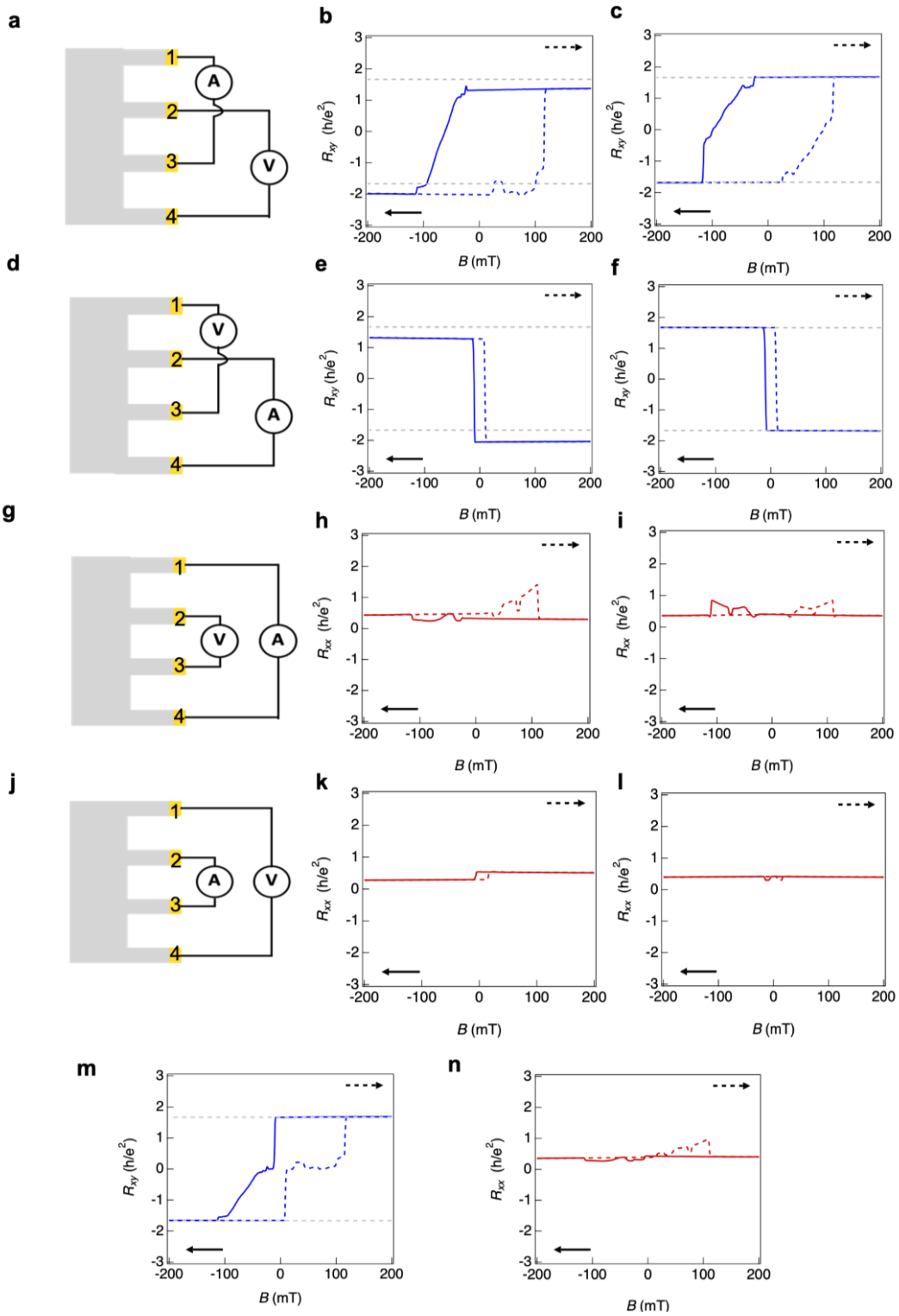

Extended Data Figure 5. Symmetrization/anti-symmetrization method to obtain magnetic hysteresis data at ν=3/5. a, b, d, e, g, h, j&k. Raw data of $R_{13,24}$, $R_{24,13}$, $R_{14,23}$ and $R_{23,14}$ measured as functions of magnetic field. The insets show the measurement pin configurations. **c, f, i&l.** R_{xy} and R_{xx} obtained after the

symmetrization process. **m&n.** R_{xy} and R_{xx} extracted after the symmetrization/anti-symmetrization process using the Onsager reciprocal relation.

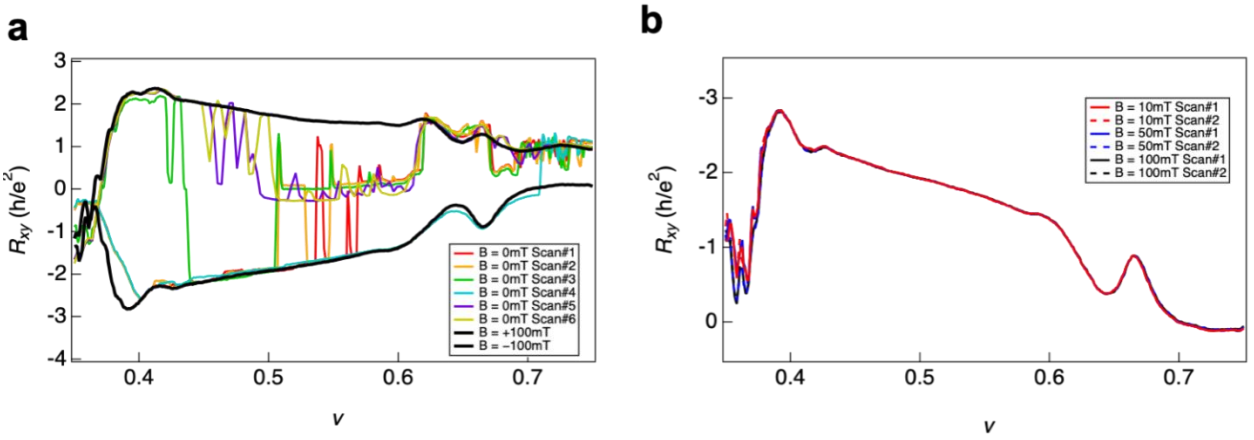

Extended Data Figure 6. R_{xy} line scans at small magnetic fields. a. R_{xy} line scan versus moiré filling factor ν at D/ε_0 = 0.9 V/nm. Curves with rainbow colors represent multiple scans at B = 0. Black curves show scans at B = ± 100 mT. **B.** R_{xy} line scans versus ν at B= 10 mT, 50 mT, 100 mT.

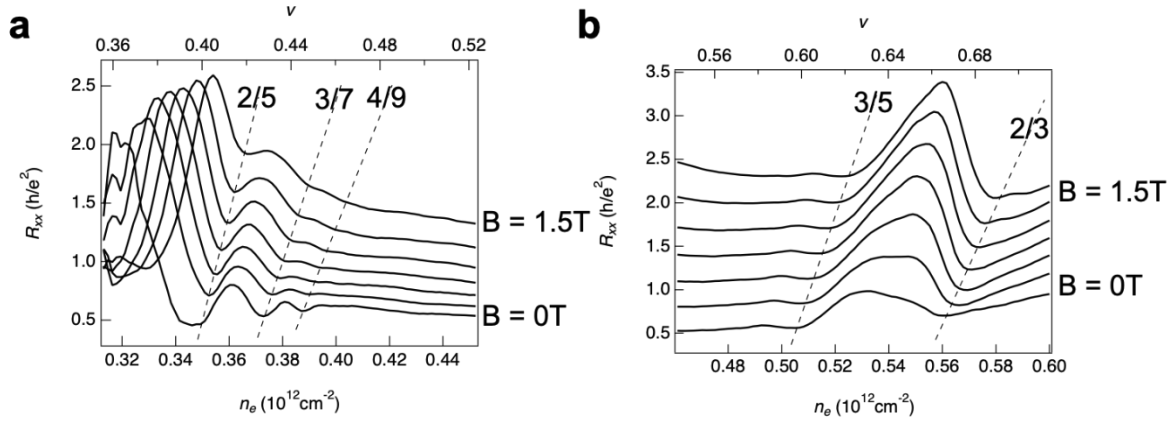

Extended Data Figure 7. R_{xx} line scans at varying magnetic field. a&b. R_{xx} line scans with moiré filling factor $\nu < 1/2$ and $\nu > 1/2$, respectively. Dips at fractional filling factors shift with magnetic field as indicated by the dashed lines. Curves are equally shifted vertically for clarity.

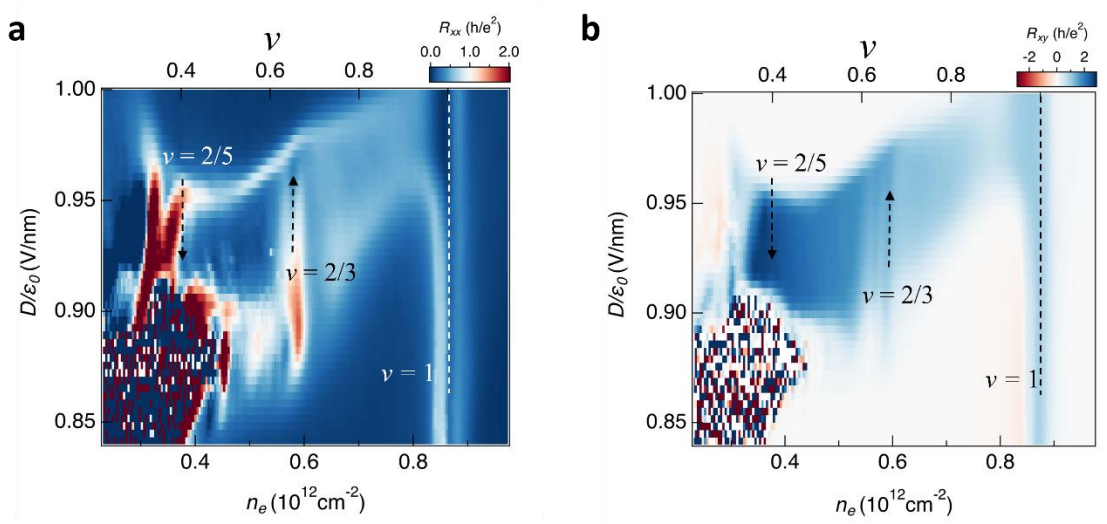

Extended Data Figure 8. Data from Device 2. a&b. Phase diagrams of the device revealed by symmetrized R_{xx} and anti-symmetrized R_{xy} at $B = \pm 0.1$ T as functions of charge density n_e (filling factor ν) and D. The temperature at the mixing chamber of dilution refrigerator is 10 mK. Clear dips of R_{xx} can be seen at filling factors of the moiré superlattice ν = 1, 2/3 and 2/5 (indicated by the dashed lines and arrows), where R_{xy} shows plateaus of values.

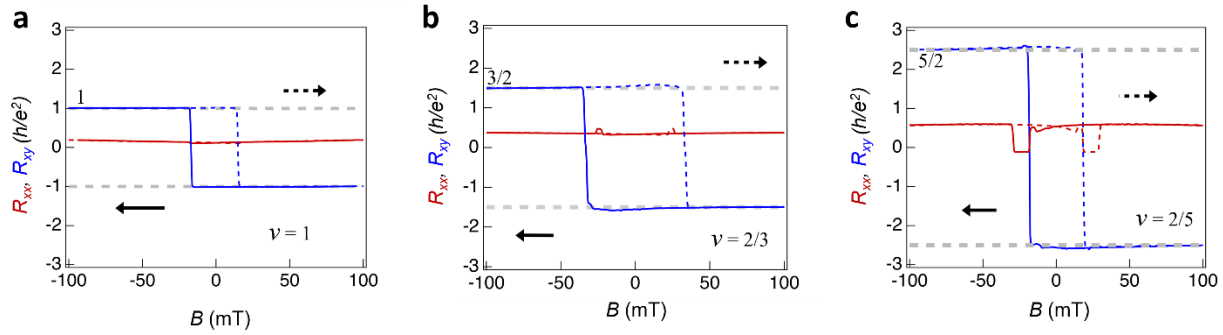

Extended Data Figure 9. Magnetic hysteresis data from Device 2. a-c. Magnetic hysteresis measurements at ν = 1, 2/3 and 2/5. Clear hysteresis and values of R_{xy} at $\frac{h}{ve^2}$ can been seen.